

# Efficient 6D Vlasov simulation using the dynamical low-rank framework **Ensign**

Fabio Cassini<sup>a,\*</sup>, Lukas Einkemmer<sup>b</sup>

<sup>a</sup>*Department of Mathematics, University of Trento, Italy*

<sup>b</sup>*Department of Mathematics, University of Innsbruck, Austria*

---

## Abstract

Running kinetic simulations using grid-based methods is extremely expensive due to the up to six-dimensional phase space. Recently, it has been shown that dynamical low-rank algorithms can drastically reduce the required computational effort, while still accurately resolving important physical features such as filamentation and Landau damping. In this paper, we introduce the **Ensign** software framework, which facilitates the efficient implementation of dynamical low-rank algorithms on modern multi-core CPU as well as GPU based systems. In particular, we illustrate its features with the help of a first-order projector-splitting integrator. Then, we propose a new second-order projector-splitting based dynamical low-rank algorithm for the full six-dimensional Vlasov–Poisson equations and implement it using our software framework. An exponential integrator based Fourier spectral method is employed to obtain a numerical method that is unconditionally stable but fully explicit. The presented numerical results demonstrate that 6D simulations can be run on a single workstation, as well as highlight the significant speedup that can be obtained using GPUs.

*Keywords:* dynamical low-rank approximation; projector-splitting algorithm; Vlasov–Poisson equation; General Purpose computing on Graphic Processing Unit (GPGPU); high-dimensional PDEs

---

## 1. Introduction

Solving kinetic equations efficiently is important in applications ranging from plasma physics to radiative transport. The main challenge in this context is the up to six-dimensional phase space and the associated unfavorable scaling of computational cost and memory requirements. Assuming  $n$  discretization points for each direction of a 6D phase space, the storage cost of a direct discretization scales as  $\mathcal{O}(n^6)$ . This is usually referred to as the curse of dimensionality.

To mitigate this issue, many techniques have been proposed in the literature; we mention, for example, particle methods [3, 36] and sparse grid approximations [19, 24]. However, it

---

\*Corresponding author

*Email addresses:* `fabio.cassini@unitn.it` (Fabio Cassini), `lukas.einkemmer@uibk.ac.at` (Lukas Einkemmer)

is well known that the former misses or underresolves some important physical phenomena (such as Landau damping or regions with low density), while the latter has issues with the Gaussian equilibrium distribution and the low regularity inherent in collisionless kinetic problems. Because of this, direct simulations are preferred and routinely conducted on large supercomputers [1, 8]. However, currently computational constraints mostly limits this to four and some five-dimensional problems.

More recently, a dynamical low-rank algorithm for solving the Vlasov–Poisson equation has been proposed in [14]. Dynamical low-rank integrators approximate the six-dimensional equation by a set of only three-dimensional advection problems. The resulting algorithm has the primary advantage of having a storage cost that scales as  $\mathcal{O}(rn^d)$ , where  $r$  is the (usually small) rank of the approximation. This can result in a drastic reduction of both memory consumption as well as computational effort. The main enabling basis for that technology was the introduction of the projector-splitting integrator [28], which allows us to obtain a robust integrator without the need for regularization within the framework of dynamical low-rank approximations [22, 27, 29, 30].

For kinetic equations the dynamical low-rank approach offers a range of advantages. In particular, filamented structures in velocity space can be resolved accurately [17]. Moreover, it is known that in the linear regime [14] and for certain fluid [9, 12] and diffusive [7, 11] limits the solution has a low-rank structure. Recently, a dynamical algorithm that is conservative from first principle has been constructed [13]. Because of these advances, dynamical low-rank approximations have received significant interest lately and methods for problems from plasma physics [14, 17, 20, 23], radiation transport [11, 26, 32, 33], and uncertainty quantification for hyperbolic problems [25] have been proposed. These schemes have the potential to enable the 6D simulation of such systems on small clusters or even desktop computers.

While mature software packages exist for solving kinetic problems using both particle methods (e.g. [2, 35]) and methods that directly discretize phase space on a grid (e.g. [10, 18, 34, 37]), no such software frameworks exist for dynamical low-rank algorithms. However, the need in the latter case is arguably even more critical, as the resulting evolution equations are usually somewhat more complex than the original model.

The purpose of this paper is to present the framework **Ensign**, which facilitates the easy and efficient implementation of dynamical low-rank algorithms for kinetic equations (both on multi-core CPU and GPU based systems). We will illustrate this by running simulations with a second-order projector-splitting dynamical low-rank algorithm based on an unconditionally stable, but still fully explicit, Fourier spectral method that we propose in this work. We emphasize, however, that our software framework is able to support other dynamical low-rank techniques (such as the unconventional integrator [4]), and is completely flexible with regards to the specific space and time discretization employed.

The remainder of the paper is structured as follows: in section 2 we provide a big picture overview of the software framework and how it can be used to implement a dynamical low-rank algorithm. Following this, the general structure underlying projector-splitting based dynamical low-rank integrators for the Vlasov–Poisson equation is described in section 3.

For the presentation and actual implementation of the proposed second-order algorithm, we rewrite the arising equations into a discrete matrix formulation, see section 4. The time and space discretization are then described in section 5. We present some numerical results in section 6 and discuss the performance of the algorithm on GPUs in section 7. Finally, we draw conclusions in section 8.

## 2. The Ensign framework and implementation

In the context of dynamical low-rank algorithms, a function  $f(t, x, v)$  is approximated as  $f(t, x, v) \approx \sum_{i,j} X_i(t, x) S_{ij}(t) V_j(t, v)$ , where the indexes  $i$  and  $j$  run from 1 to  $r$  and  $r$  the chosen approximation rank. The quantities  $X_i(t, x)$ ,  $S_{ij}(t)$  and  $V_j(t, v)$  constitute the so called low-rank factors and, after discretization in  $x$  and  $v$ , they can be expressed as matrices (see sections 3 and 4 for more details). Therefore, independently of the specific case under consideration, the common key point for an efficient implementation of dynamical low-rank algorithms for kinetic equations, both on CPU and GPU based systems, is the fast computation of matrix-matrix and matrix-vector products. For every modern computer architecture, we have at our disposal heavily optimized routines to perform such operations, usually referred to as BLAS routines. For example, Intel MKL [5] or OpenBLAS [38] are available for CPU based systems while we have cuBLAS [6] and MAGMA [31] for NVIDIA GPUs. Among their many features, all these libraries are equipped with multithreaded versions of the BLAS routines.

The main idea behind **Ensign** is to provide the user a collection of structures and functions in order to compute and manipulate *easily* the arising quantities in dynamical low-rank algorithms (functions to compute the needed coefficients and wrappers to the just mentioned BLAS routines, for example). Our framework, which is publicly available at <https://github.com/leinkemmer/Ensign> under the MIT license, is written in the C++ programming language and uses CUDA for the GPU implementation.

We now illustrate some of its features with a simple example in the context of dynamical low-rank projector-splitting algorithms for the Vlasov–Poisson equations. A reader not familiar with this kind of integrators can find more details in section 3 and 4. A (first order) dynamical low-rank projector-splitting algorithm for Vlasov–Poisson equation is sketched in Algorithm 1. For a 6D problem, the lines rewritten in source code (i.e. the ones colored in orange in Algorithm 1) are given in Figure 1, which basically illustrates how the steps arising from the mathematical equations can be directly translated into the functions provided by our framework.

In terms of data storage, we employ a user-defined structure `multi_array` which lets us easily define vectors (`w_v1`, for example) and matrices (`V0`, for example) both in CPU and in GPU memory, depending on the need. This structure is also enriched with some user-friendly functions and operators which are useful to perform basic operations between `multi_arrays`, such as sum, difference, multiplication with a scalar, and to transfer data from/to CPU/GPU memory (the latter is simply done by assignment).

The input matrices (2D `multi_arrays`) `X0`, `S0` and `V0` reflect the evaluation of the low-rank factors on a discretized grid. In particular, the degrees of freedom are linearized so that

---

**Algorithm 1:** Sketch of the first order dynamical low-rank projector-splitting algorithm. The orange colored instructions, which are largely problem independent, are translated into source code in Figure 1.

---

**Input:**  $X^0 \in \mathbb{R}^{N_x \times r}$ ,  $S^0 \in \mathbb{R}^{r \times r}$ ,  $V^0 \in \mathbb{R}^{N_v \times r}$

**Output:**  $X^1 \in \mathbb{R}^{N_x \times r}$ ,  $S^3 \in \mathbb{R}^{r \times r}$ ,  $V^1 \in \mathbb{R}^{N_v \times r}$

- 1 Compute  $C$  coefficients;
  - 2 Compute  $K^0$ ;
  - 3 Compute electric field  $E^0$ ;
  - 4 Solve evolution equation for  $K$  to obtain  $K^1$ ;
  - 5 Perform QR decomposition of  $K^1$  to obtain  $X^1$  and  $S^1$ ;
  - 6 Compute  $D$  coefficients;
  - 7 Solve evolution equation for  $S$  to obtain  $S^2$ ;
  - 8 Compute  $L^0$ ;
  - 9 Solve evolution equation for  $L$  to obtain  $L^1$ ;
  - 10 Perform QR decomposition of  $L^1$  to obtain  $V^1$  and  $S^3$ ;
- 

each column corresponds to the discretized version of a single low-rank factor. For example, the initialization of the first column of the matrix `X0` (2D `multi_array`) corresponding to a low-rank factor  $\ell(x_1, x_2, x_3)$  can be performed in C++ as presented in Figure 2. There, the number of discretization points for each direction is stored in the array `N_xx`, the left extremes in `lim_xx` and the grid spacing in `h_xx`. While this specific example is presented in the context of a uniform space discretization, any other kind of discretization (with an arbitrary ordering of the nodes) would work in a straightforward way as well.

We use C++ templates in order to abstract the underlying architecture on which the code is run. Depending on whether a function (such as a matrix operation) is called with arguments that reside on the CPU or on the GPU, an efficient implementation suitable for that hardware architecture is selected. Indeed, whether the code runs on the CPU or on the GPU is never explicitly specified in the code example in Figure 1, because it is automatically detected from the storage location of the input arguments of the functions. Thus, the algorithmic part of the implementation is completely independent of what computer hardware the code is eventually run on.

Concerning BLAS operations, *Ensign* provides the structure `blas_ops` which contains wrappers for matrix multiplications (e.g. `matmul` and `matmul_transb`) and handles needed to call properly these routines on the GPU. Then, our framework is equipped with a function to compute the  $C$  and  $D$  integral coefficients, namely `coeff`. Depending on the input matrices and the vector of weights, the function computes the corresponding matrix of coefficients. For example, given the 1D quadrature weight `multi_array` `w_v1` and the 2D `multi_array` `V0`, the coefficient matrix  $C_{1,v_1}$  is computed as in line 3 of Figure 1. Moreover, we can find in our framework the structure `gram_schmidt` which contains a function to compute the QR decomposition. It is based on a modified Gram Schmidt algorithm written in matrix formulation, so that again the internal computations are automatically performed in parallel

by means of calls to BLAS routines. For example, given the 2D `multi_arrays` `K1` and `S1` and a function `ip_xx` which computes the inner product, the call to perform the QR decomposition of `K1` is given in line 16 of Figure 1.

Finally, we want to emphasize that while we have illustrated our software framework for a simple projector-splitting based dynamical low-rank integrator, every effort has been made in designing `Ensign` to allow also the implementation of other dynamical low-rank integrators, such as the recently proposed unconventional integrator [4] or the conservative dynamical low-rank integrator [13]. Moreover, we point out that the user is completely free to choose any space or time discretization appropriate to the problem. The only requirement in terms of space discretization is that the degrees of freedom of the low-rank factors have to be collected in suitable matrices by means of an index linearization (see for example the code in Figure 2). This is certainly possible for all the commonly used space discretization strategies.

### 3. Low-rank approximation for the Vlasov–Poisson equation

In this paper we consider the Vlasov–Poisson equation in dimensionless form given by

$$\begin{cases} \partial_t f(t, x, v) + v \cdot \nabla_x f(t, x, v) - E(f)(t, x) \cdot \nabla_v f(t, x, v) = 0, \\ E(f)(t, x) = -\nabla_x \phi(t, x) \\ -\Delta \phi(t, x) = \rho(f)(t, x) + 1, \quad \rho(f)(t, x) = -\int_{\Omega_v} f(t, x, v) dv, \end{cases} \quad (1)$$

where  $f(t, x, v)$  represents the particle-density function of the species under consideration,  $t \in \mathbb{R}_0^+$  is the time variable,  $x \in \Omega_x \subset \mathbb{R}^d$  refers to the space variable,  $v \in \Omega_v \subset \mathbb{R}^d$  is the velocity variable and  $d = 1, 2, 3$ . Depending on the physical phenomenon under study, system (1) is completed with appropriate boundary and initial conditions.

We now describe how to obtain the dynamical low-rank approximation of the Vlasov–Poisson system (1). For more details, we refer the reader to [14].

The computational domain is denoted by  $\Omega = \Omega_x \times \Omega_v$ . Then, instead of solving directly (1), we look for an approximation of the particle-density function  $f(t, x, v)$  that, for fixed  $t$ , lies in the rank- $r$  manifold

$$\mathcal{M} = \left\{ g(x, v) \in L^2(\Omega) : g(x, v) = \sum_{i,j} X_i(x) S_{ij} V_j(v) \text{ with invertible } S = (S_{ij}) \in \mathbb{R}^{r \times r}, \right. \\ \left. X_i \in L^2(\Omega_x), V_j \in L^2(\Omega_v) \text{ with } \langle X_i, X_k \rangle_x = \delta_{ik}, \langle V_j, V_\ell \rangle_v = \delta_{j\ell} \right\}$$

with corresponding tangent space

$$\mathcal{T}_f \mathcal{M} = \left\{ \dot{g}(x, v) \in L^2(\Omega) : \dot{g}(x, v) = \sum_{i,j} (X_i(x) \dot{S}_{ij} V_j(v) + \dot{X}_i(x) S_{ij} V_j(v) + X_i(x) S_{ij} \dot{V}_j(v)), \right. \\ \left. \text{with } \dot{S} \in \mathbb{R}^{r \times r}, \dot{X}_i \in L^2(\Omega_x), \dot{V}_j \in L^2(\Omega_v) \text{ and } \langle X_i, \dot{X}_k \rangle_x = 0, \langle V_j, \dot{V}_\ell \rangle_v = 0 \right\}.$$

Here  $\langle \cdot, \cdot \rangle_x$  and  $\langle \cdot, \cdot \rangle_v$  denote the standard inner products on  $L^2(\Omega_x)$  and  $L^2(\Omega_v)$ , respectively, while the dot stands for the time derivative. Moreover, all indexes run from 1 to  $r$  and, for simplicity of presentation, we drop these limits from the notation.

To obtain the dynamical low-rank approximation of the Vlasov–Poisson system (1) we need to solve

$$\partial_t f(t, x, v) = -P(f)(v \cdot \nabla_x f(t, x, v) - E(f) \cdot \nabla_v f(t, x, v)),$$

where  $P(f)$  is the orthogonal projector onto the tangent space  $\mathcal{T}_f \mathcal{M}$ . For simplicity of notation, we will from now on use  $f$  to denote the low-rank approximation to the particle-density. The orthogonal projection of a generic function  $g$  can be written as

$$P(f)g = P_{\nabla} g - P_{\nabla} P_{\overline{X}} g + P_{\overline{X}} g$$

where  $P_{\overline{X}}$  and  $P_{\nabla}$  are orthogonal projectors onto the spaces spanned by the functions  $X_i$  and  $V_j$ , respectively. This formulation suggests a three-term splitting with subflows given by

$$\partial_t f(t, x, v) = -P_{\nabla}(v \cdot \nabla_x f(t, x, v) - E(f) \cdot \nabla_v f(t, x, v)), \quad (2)$$

$$\partial_t f(t, x, v) = P_{\nabla} P_{\overline{X}}(v \cdot \nabla_x f(t, x, v) - E(f) \cdot \nabla_v f(t, x, v)), \quad (3)$$

$$\partial_t f(t, x, v) = -P_{\overline{X}}(v \cdot \nabla_x f(t, x, v) - E(f) \cdot \nabla_v f(t, x, v)). \quad (4)$$

This is the projector-splitting integrator that has been first proposed in [28].

By explicitly applying the projector  $P_{\nabla}$  on equation (2), we can see that solving (2) is equivalent to

$$\begin{cases} \partial_t K_j(t, x) = -\sum_{\ell} c_{j\ell}^1 \cdot \nabla_x K_{\ell}(t, x) + \sum_{\ell} c_{j\ell}^2 \cdot E(K)(t, x) K_{\ell}(t, x), \\ V_j(t, v) = \tilde{V}_j(v), \end{cases} \quad (5)$$

where the approximate particle-density function is written as

$$f(t, x, v) = \sum_j K_j(t, x) V_j(t, v), \quad K_j(t, x) = \sum_i X_i(t, x) S_{ij}(t)$$

and

$$c_{j\ell}^1 = \int_{\Omega_v} v \tilde{V}_j(v) \tilde{V}_{\ell}(v) dv, \quad c_{j\ell}^2 = \int_{\Omega_v} \tilde{V}_j(v) \nabla_v \tilde{V}_{\ell}(v) dv.$$

Equation (5) is usually referred to as the *K step* of the low-rank projector splitting algorithm. Note that the velocity dependent low-rank factors, i.e.  $V_j$ , do not change during this step. That is, we can use their value at the beginning of the step, i.e.  $\tilde{V}_j$ , in all computations.

The second subflow (3), by applying both projectors  $P_{\nabla}$  and  $P_{\overline{X}}$ , can be written as

$$\begin{cases} \dot{S}_{ij}(t) = \sum_{k,\ell} (c_{j\ell}^1 \cdot d_{ik}^2 - c_{j\ell}^2 \cdot d_{ik}^1 [E(S)]) S_{k\ell}(t), \\ X_i(t, x) = \check{X}_i(x), \\ V_j(t, v) = \tilde{V}_j(v), \end{cases} \quad (6)$$

where

$$d_{ik}^1[E(S)] = \int_{\Omega_x} \check{X}_i(x)E(S)\check{X}_k(x)dx, \quad d_{ik}^2 = \int_{\Omega_x} \check{X}_i(x)\nabla_x\check{X}_k(x)dx.$$

We refer to (6) as the *S step* of the low-rank projector splitting algorithm. Note that neither  $X_i$  nor  $V_j$  change during this step.

Finally, we can demonstrate that solving (4) is equivalent to

$$\begin{cases} \partial_t L_i(t, v) = \sum_k d_{ik}^1[E(L)] \cdot \nabla_v L_k(t, v) - \sum_k (d_{ik}^2 \cdot v) L_k(t, v), \\ X_i(t, x) = \check{X}_i(x). \end{cases} \quad (7)$$

with the approximate particle-density function written as

$$f(t, x, v) = \sum_i X_i(t, x)L_i(t, v), \quad L_i(t, v) = \sum_j S_{ij}(t)V_j(t, v).$$

This step of the low-rank projector splitting algorithm is referred to as the *L step*. Note that  $X_i$  does not change during this step.

Concerning the equations of the electric field, they can be written in terms of the low-rank factors  $X_i(t, x)$ ,  $S_{ij}(t)$  and  $V_j(t, v)$  as well. Indeed, we can express the charge density  $\rho(f)(t, x)$  as

$$\begin{aligned} \rho(K)(t, x) &= - \sum_j K_j(t, x)\rho(\tilde{V}_j(v)), & \rho(\tilde{V}_j(v)) &= \int_{\Omega_v} \tilde{V}_j(v) dv, \\ \rho(S)(t, x) &= - \sum_{i,j} \check{X}_i(x)S_{ij}(t)\rho(\tilde{V}_j(v)), \\ \rho(L)(t, x) &= - \sum_i \check{X}_i(x)\rho(L_i(t, v)), & \rho(L_i(t, v)) &= \int_{\Omega_v} L_i(t, v) dv, \end{aligned}$$

depending on the need.

Finally, the approximate solution to (1) is recovered by combining the partial solutions of the *K*, *S* and *L* step by splitting. In the easiest setting the first order Lie splitting scheme solves the three subflows in sequence. We will later on also outline a second order scheme based on Strang splitting.

#### 4. Matrix formulation of the discrete algorithm

So far we have considered the low-rank approximation in a continuous framework. However, to perform calculations on a computer we have to discretize the equations for the *K*, *S*, and *L* step. In this section, we assume that a space discretization has been chosen. Our goal is then to collect the degrees of freedom into matrices and write the resulting operations (as much as possible) as matrix-matrix and matrix-vector operations. This allows us to use the software framework described in section 2 in order to obtain an efficient implementation with minimal effort by the programmer.

We consider  $n_{x_i}$  discretization points for the space variable  $x_k$ ,  $k = 1, \dots, d$  and  $n_{v_k}$  discretization points for the velocity variable  $v_k$ ,  $k = 1, \dots, d$ . The total number of degrees of freedom is denoted as  $N_x = n_{x_1} \cdots n_{x_d}$  and  $N_v = n_{v_1} \cdots n_{v_d}$  for space and velocity, respectively. Then, for a fixed time  $t$ , we define  $X = [X_1, \dots, X_r] \in \mathbb{R}^{N_x \times r}$  to be the matrix having on the columns the evaluation of the low-rank factors  $X_i$  on the chosen spatial grid. Clearly, the resulting matrix entries depend on the discretization performed and on the ordering of the grid points. Similarly, we consider  $V = [V_1, \dots, V_r] \in \mathbb{R}^{N_v \times r}$  to be the matrix having on the columns the evaluation of the low-rank factors  $V_j$  on the velocity grid. The coupling coefficients  $S_{ij}$  are collected in the matrix  $S \in \mathbb{R}^{r \times r}$ . Hence, we can write the evolution equation for the  $K$  step (5) in matrix formulation as follows

$$\partial_t K(t) = - \sum_{i=1}^d \bar{\partial}_{x_i} K(t) C_{1,v_i}^\top + \sum_{i=1}^d \text{diag}(E_{x_i}(K(t))) K(t) C_{2,v_i}^\top \quad (8)$$

where

$$\begin{aligned} K(t) &= X(t)S(t), \quad K(t) \in \mathbb{R}^{N_x \times r}, \\ C_{1,v_i} &= \tilde{V}^\top \text{diag}(\omega_{1,v_i}) \tilde{V} \in \mathbb{R}^{r \times r}, \\ C_{2,v_i} &= \tilde{V}^\top \text{diag}(\omega_{2,v_i}) \bar{\partial}_{v_i} \tilde{V} \in \mathbb{R}^{r \times r} \end{aligned}$$

and the  $i$ th component of the electric field has been denoted by  $E_{x_i}(K(t)) \in \mathbb{R}^{N_x}$ . In addition, we have used  $\bar{\partial}_{x_i}$  to denote the discretization of the spatial derivative operator. While this operator can be represented as a matrix, in many cases it is more efficient to directly compute its application to  $K(t)$  (e.g. in a stencil code or by using FFTs). We also note that in order to compute the coefficients  $C_{1,v_i}$  and  $C_{2,v_i}$  it would (obviously) be very inefficient to form the diagonal matrix. Instead, our framework provides the function `coeff` that takes the matrices as well as a vector of weights as input and computes the corresponding quadrature (see Figure 1).

For the evolution equation of the S step (6) we obtain

$$\dot{S}(t) = \sum_{i=1}^d D_{2,x_i} S(t) C_{1,v_i}^\top - \sum_{i=1}^d D_{1,x_i} [E(S(t))] S(t) C_{2,v_i}^\top. \quad (9)$$

where

$$\begin{aligned} D_{1,x_i} [E(S(t))] &= \check{X}^\top \text{diag}(\omega_{1,x_i}^E) \check{X} \in \mathbb{R}^{r \times r}, \\ D_{2,x_i} &= \check{X}^\top \text{diag}(\omega_{2,x_i}) \bar{\partial}_{x_i} \check{X} \in \mathbb{R}^{r \times r}. \end{aligned}$$

Finally, for the evolution equation of the L step (7) we have

$$\partial_t L(t) = \sum_{i=1}^d \bar{\partial}_{v_i} L(t) D_{1,x_i}^\top - \sum_{i=1}^d \text{diag}(\bar{v}_i) L(t) D_{2,x_i}^\top \quad (10)$$

where

$$L(t) = V(t)S(t)^\top, \quad L(t) \in \mathbb{R}^{N_v \times r}$$



and  $\bar{v}_i \in \mathbb{R}^{N_v}$  is the vector with the positions of the grid points in velocity space.

The equations for the electric field are given by

$$\begin{aligned} (E_{x_1}(f)(t), \dots, E_{x_d}(f)(t)) &= -\nabla_x \Phi(f)(t), \quad E_{x_i}(f)(t) \in \mathbb{R}^{N_x}, \quad \Phi(f)(t) \in \mathbb{R}^{N_x} \\ -\Delta \Phi(f)(t) &= P(f)(t) + 1, \quad P(f)(t) \in \mathbb{R}^{N_x} \end{aligned}$$

where the discretized charge density  $P(f)(t)$  can be computed in terms of the low-rank factors, depending on the need, as

$$P(K)(t) = -K(t)\tilde{P}, \quad \tilde{P} = \tilde{V}^\top \omega_v \in \mathbb{R}^r, \quad \omega_v \in \mathbb{R}^{N_v} \quad (11)$$

$$P(S)(t) = -\check{X}S(t)\tilde{P},$$

$$P(L)(t) = -\check{X}\bar{P}(L(t)), \quad \bar{P}(L(t)) = L(t)^\top \omega_v \in \mathbb{R}^r, \quad (12)$$

Let us also note that the approximation of the particle density function can be recovered at any moment from the low-rank factors by computing

$$F(t) = X(t)S(t)V(t)^\top \in \mathbb{R}^{N_x \times N_v},$$

but clearly this is not needed for the low-rank projector splitting algorithm, and doing so would be extremely costly.

#### 4.1. Order 1 low-rank projector-splitting algorithm

The solutions of the subflows corresponding to the  $K$  step, the  $S$  step, and the  $L$  step are then combined by a splitting scheme in order to recover an approximation of the particle density function. In order to obtain a first order method it is sufficient to consider a Lie–Trotter splitting algorithm. A detailed description of the resulting scheme is given in Algorithm 2.

---

**Algorithm 2:** First order accurate Lie splitting integrator for (1).

---

**Input:**  $X^0, S^0, V^0$  such that  $f(0, x, v) \approx \sum_{i,j} X_i^0(x)S_{ij}^0 V_j^0(v)$ , timestep size  $\tau$

**Output:**  $X^1, S^1, V^1$  such that  $f(\tau, x, v) \approx \sum_{i,j} X_i^1(x)S_{ij}^1 V_j^1(v)$

- 1 Compute  $C_{1,v_i}$  and  $C_{2,v_i}$ ,  $i = 1, \dots, d$ , using  $V^0$ ;
  - 2 Compute  $K^0$  using  $X^0$  and  $S^0$ ;
  - 3 Compute the electric field  $E^0$  with (11) using  $K^0$  and  $V^0$ ;
  - 4 Solve (8) with initial value  $K^0$  and  $E^0$  up to time  $\tau$  to obtain  $K^1$ ;
  - 5 Perform a QR decomposition of  $K^1$  to obtain  $X^1$  and  $S^1$ ;
  - 6 Compute  $D_{1,x_i}$  and  $D_{2,x_i}$ ,  $i = 1, \dots, d$ , using  $E^0$  and  $X^1$ ;
  - 7 Solve (9) with initial value  $S^1$  and  $E^0$  up to time  $\tau$  to obtain  $S^2$ ;
  - 8 Compute  $L^0$  using  $V^0$  and  $S^2$ ;
  - 9 Solve (10) with initial value  $L^0$  and  $E^0$  up to time  $\tau$  to obtain  $L^1$ ;
  - 10 Perform a QR decomposition of  $L^1$  to obtain  $V^1$  and  $S^3$ ;
-

We remark that the computation of the electric field is performed only once at the beginning of the time step. This is not a restriction in the context of a Lie–Trotter splitting, as fixing the electric field for each time step still results in a first order approximation. After performing the  $K$  and the  $L$  steps, in order to proceed with the algorithm, we need to recover the orthonormal functions  $X_i$ ,  $V_j$  and the coupling coefficients  $S_{ij}$ . This can be accomplished, for example, by a QR or an SVD decomposition. In principle, any numerical method can be employed to integrate in time (8)–(10). We will discuss our proposal, based on the choice of a spectral phase space discretization, in section 5.

#### 4.2. Order 2 low-rank projector-splitting algorithm

A straightforward generalization to a second order integrator by employing a Strang splitting procedure instead of a Lie–Trotter one is not possible. Indeed, if we freeze the electric field at the beginning of the time step, we still end up with a first order algorithm. To overcome this problem, an almost symmetric Strang splitting scheme is proposed in [14]; however, in order to achieve full second order, that algorithm requires several updates of the electric field, which in turn translates into high computational effort. We propose here a slightly different strategy to obtain a second order scheme, listed in detail in Algorithm 3. The underlying idea is that we compute an approximation of the electric field at time  $\tau/2$  of (local) second order by means of Algorithm 2. Then, we restart the integration with a classic Strang splitting scheme employing as constant electric field the approximation at the half step. Mathematically, this can be analyzed as an almost symmetric splitting scheme, see [15, 16].

### 5. Time and space discretization of $K$ , $S$ and $L$ steps

As already mentioned in section 4, in principle any numerical scheme can be used to integrate equations (8)–(10) in time. However, depending on the selected phase-space discretization, some choices can be more adequate than others. In particular, we describe here in detail a strategy which uses a Fourier spectral discretization for both space and velocity variables. The method converges rapidly in space and velocity (owing to the spectral discretization) and despite being fully explicit does not suffer from a stability induced stepsize restriction in time.

Let us consider the  $K$  step (8). For clarity of exposition we will only consider the three dimensional case here. By performing a further splitting of the  $K$  step we obtain the following three subflows

$$\begin{aligned}\partial_t K_1(t) &= -\bar{\partial}_{x_1} K_1(t) C_{1,v_1}^\top, \\ \partial_t K_2(t) &= -\bar{\partial}_{x_2} K_2(t) C_{1,v_2}^\top, \\ \partial_t K_3(t) &= -\bar{\partial}_{x_3} K_3(t) C_{1,v_3}^\top + \sum_{i=1}^3 \text{diag}(E_{x_i}) K(t) C_{2,v_i}^\top.\end{aligned}$$

---

**Algorithm 3:** Second order accurate integrator for (1). Steps 1–9 correspond to a Lie splitting integration with Algorithm 2 and timestep size  $\tau/2$ .

---

**Input:**  $X^0, S^0, V^0$  such that  $f(0, x, v) \approx \sum_{i,j} X_i^0(x) S_{ij}^0 V_j^0(v)$ , timestep size  $\tau$

**Output:**  $X^3, S^7, V^1$  such that  $f(\tau, x, v) \approx \sum_{i,j} X_i^3(x) S_{ij}^7 V_j^1(v)$

- 1 Compute  $C_{1,v_i}$  and  $C_{2,v_i}$ ,  $i = 1, \dots, d$ , using  $V^0$ ;
  - 2 Compute  $K^0$  using  $X^0$  and  $S^0$ ;
  - 3 Compute the electric field  $E^0$  with (11) using  $K^0$  and  $V^0$ ;
  - 4 Solve (8) with initial value  $K^0$  and  $E^0$  up to time  $\tau/2$  to obtain  $K^1$ ;
  - 5 Perform a QR decomposition of  $K^1$  to obtain  $X^1$  and  $S^1$ ;
  - 6 Compute  $D_{1,x_i}$  and  $D_{2,x_i}$ ,  $i = 1, \dots, d$ , using  $E^0$  and  $X^1$ ;
  - 7 Solve (9) with initial value  $S^1$  and  $E^0$  up to time  $\tau/2$  to obtain  $S^2$ ;
  - 8 Compute  $L^0$  using  $V^0$  and  $S^2$ ;
  - 9 Solve (10) with initial value  $L^0$  and  $E^0$  up to time  $\tau/2$  to obtain  $L^1$ ;
  - 10 Compute the electric field  $E^{1/2}$  with (12) using  $X^1$  and  $L^1$ ;
  - 11 Solve (8) with initial value  $K^0$  and  $E^{1/2}$  up to time  $\tau/2$  to obtain  $K^2$ ;
  - 12 Perform a QR decomposition of  $K^2$  to obtain  $X^2$  and  $S^3$ ;
  - 13 Compute  $D_{1,x_i}$  and  $D_{2,x_i}$ ,  $i = 1, \dots, d$ , using  $E^{1/2}$  and  $X^2$ ;
  - 14 Solve (9) with initial value  $S^3$  and  $E^{1/2}$  up to time  $\tau/2$  to obtain  $S^4$ ;
  - 15 Compute  $L^1$  using  $V^0$  and  $S^4$ ;
  - 16 Solve (10) with initial value  $L^1$  and  $E^{1/2}$  up to time  $\tau$  to obtain  $L^2$ ;
  - 17 Perform a QR decomposition of  $L^2$  to obtain  $V^1$  and  $S^5$ ;
  - 18 Compute  $C_{1,v_i}$  and  $C_{2,v_i}$ ,  $i = 1, \dots, d$ , using  $V^1$ ;
  - 19 Solve (9) with initial value  $S^5$  and  $E^{1/2}$  up to time  $\tau/2$  to obtain  $S^6$ ;
  - 20 Compute  $K^3$  using  $X^2$  and  $S^6$ ;
  - 21 Solve (8) with initial value  $K^3$  and  $E^{1/2}$  up to time  $\tau/2$  to obtain  $K^4$ ;
  - 22 Perform a QR decomposition of  $K^4$  to obtain  $X^3$  and  $S^7$ ;
-

Applying a Fourier transform in the  $x_i$  variables (denoted by  $\mathcal{F}_{x_i}$ ),  $i = 1, 2, 3$ , we obtain

$$\begin{aligned}\partial_t \hat{K}_1(t) &= -D_{x_1}^{\mathcal{F}} \hat{K}_1(t) C_{1,v_1}^{\top}, \\ \partial_t \hat{K}_2(t) &= -D_{x_2}^{\mathcal{F}} \hat{K}_2(t) C_{1,v_2}^{\top}, \\ \partial_t \hat{K}_3(t) &= -D_{x_3}^{\mathcal{F}} \hat{K}_3(t) C_{1,v_3}^{\top} + \sum_{i=1}^3 \mathcal{F}_{x_3}(\text{diag}(E_{x_i})K(t)) C_{2,v_i}^{\top},\end{aligned}$$

where  $D_{x_i}^{\mathcal{F}}$  is a diagonal matrix containing the coefficients stemming from the differential operator  $\partial_{x_i}$  in Fourier space. Then, as the matrices  $C_{1,v_i}^{\top}$  are symmetric by construction, it is possible to diagonalize them so that  $C_{1,v_i}^{\top} = T_{v_i} D_{v_i} T_{v_i}^{\top}$ . We note that this is computationally cheap as these are only  $r \times r$  matrices. By performing the substitution  $\hat{M}_i(t) = \hat{K}_i(t) T_{v_i}$  we have

$$\partial_t \hat{M}_1(t) = -D_{x_1}^{\mathcal{F}} \hat{M}_1(t) D_{v_1} \tag{13}$$

$$\partial_t \hat{M}_2(t) = -D_{x_2}^{\mathcal{F}} \hat{M}_2(t) D_{v_2} \tag{14}$$

$$\partial_t \hat{M}_3(t) = -D_{x_3}^{\mathcal{F}} \hat{M}_3(t) D_{v_3} + \sum_{i=1}^3 \mathcal{F}_{x_3}(\text{diag}(E_i)K(t)) C_{2,v_i}^{\top} T_{v_3} \tag{15}$$

At this point, equations (13) and (14) can be solved exactly in time by means of independent pointwise operations, while (15) can be solved efficiently by means of a second order Runge–Kutta exponential integrator (see [21] for a survey), again just using independent pointwise operations. We choose to use exponential integrators in the time evolution of this step because in this way we remove any CFL-like restriction of the stepsize coming from the stiffness of the spatial derivative. Moreover, as everything is written in terms of independent pointwise operations, the integration of the single subflow can be performed completely in parallel.

Finally, coming back to the original variables  $\hat{K}_i$  and performing an inverse Fourier transform, allows us to obtain an approximate solutions for the subflows. Embedding this procedure in a splitting context returns the desired approximation of the evolution equation for the  $K$  step. In particular, for the first order method described in Algorithm 2 it is enough to perform a Lie–Trotter splitting, while a Strang splitting procedure is needed for the second order method presented in Algorithm 3.

Concerning the integration of the evolution equation of the  $L$  step (10), similar considerations apply. Finally, concerning the  $S$  step (9), it is an  $r \times r$  problem and there is no source of stiffness in it. Hence, we perform its time integration by means of the classical explicit fourth order Runge–Kutta scheme RK4.

## 6. Numerical experiments

In this section we will present some numerical results and validate the implementation of the algorithm described in section 4. The developed code solves the 6D Vlasov–Poisson

equation and uses the framework **Ensign**. All the experiments in this section have been performed with the aid of a single NVIDIA Tesla A100 card (theoretical peak memory bandwidth of 1555 GB/s and peak floating point processing power for double precision of 9.7 TFlops) with 40 GB of RAM.

### 6.1. Orders of convergence

First, we check the implementation of the low-rank projector-splitting algorithms by computing numerically the order of convergence of the methods. For this purpose, we consider a 6D linear Landau damping problem posed on the domain  $\Omega = (0, 4\pi)^3 \times (-6, 6)^3$  with an initial particle-density given by

$$f_0(x_1, x_2, x_3, v_1, v_2, v_3) = \frac{1}{\sqrt{(2\pi)^3}} e^{-(v_1^2+v_2^2+v_3^2)/2} (1 + \alpha_1 \cos(\kappa_1 x_1) + \alpha_2 \cos(\kappa_2 x_2) + \alpha_3 \cos(\kappa_3 x_3)). \quad (16)$$

The parameters are set to  $\alpha_1 = \alpha_2 = \alpha_3 = 10^{-2}$  and  $\kappa_1 = \kappa_2 = \kappa_3 = \frac{1}{2}$ . We consider the problem with periodic boundary conditions in all directions and integrate it up to final time  $T = 1$ . Concerning the space discretization, we take  $32^3$  as number of discretization points for both space and velocity variables. The rank of the solution is fixed to  $r = 10$ . As a reference solution, we take the result of the second order low-rank projector-splitting algorithm with  $m = 2000$  timesteps (time step size  $\tau = 5 \cdot 10^{-4}$ ).

We also consider also a 6D two stream instability defined on the domain  $\Omega = (0, 10\pi)^3 \times (-9, 9)^3$  with initial distribution

$$\begin{aligned} f_0(x_1, x_2, x_3, v_1, v_2, v_3) = & \frac{1}{\sqrt{(8\pi)^3}} \left( e^{-(v_1 - \bar{v}_1)^2/2} + e^{-(v_1 + \bar{v}_1)^2/2} \right) \\ & \times \left( e^{-(v_2 - \bar{v}_2)^2/2} + e^{-(v_2 + \bar{v}_2)^2/2} \right) \\ & \times \left( e^{-(v_3 - \bar{v}_3)^2/2} + e^{-(v_3 + \bar{v}_3)^2/2} \right) \\ & \times (1 + \alpha_1 \cos(\kappa_1 x_1) + \alpha_2 \cos(\kappa_2 x_2) + \alpha_3 \cos(\kappa_3 x_3)). \end{aligned} \quad (17)$$

In this case the parameters are given by  $\alpha_1 = \alpha_2 = \alpha_3 = 10^{-3}$ ,  $\kappa_1 = \kappa_2 = \kappa_3 = \frac{1}{5}$ ,  $\bar{v}_1 = \frac{5}{2}$ ,  $\bar{v}_2 = \bar{v}_3 = 0$ ,  $\tilde{v}_1 = -\frac{5}{2}$ ,  $\tilde{v}_2 = -\frac{9}{4}$  and  $\tilde{v}_3 = -2$ . As for linear Landau damping, the problem is equipped with period boundary conditions in all directions and the rank is fixed to  $r = 10$ . We perform simulations up to final time  $T = \frac{1}{20}$  with  $32^3$  discretization points for both space and velocity variables. We again consider as a reference solution the results of the second order algorithm with  $m = 2000$  timesteps (timestep size  $\tau = 2.5 \cdot 10^{-5}$ ).

The results for both problems are collected in Figure 3. In each of the two cases, we can clearly see that the first and second order algorithms show the expected order of convergence.

### 6.2. Linear Landau simulation

We consider again the 6D linear Landau (16) with periodic boundary conditions and the same set of parameters. However, now we pick  $64^3$  discretization points for the space

variables and  $256^3$  for the velocity ones. We integrate the problem with the second order scheme until  $T = 60$  with timestep size  $\tau = 10^{-2}$ . The approximation rank is fixed to  $r = 10$ .

We emphasize that a direct (Eulerian or semi-Lagrangian) Vlasov solver would require at least 70 TB of main memory (RAM) to perform these simulations, which would clearly only be feasible on a supercomputer. Our dynamical low-rank simulation, in contrast, runs on a single A100 with 40 GB of memory and takes approximately an hour.

The results of the simulation, in terms of electric energy, error in mass and error in total energy, are summarized in Figure 4. We can observe that the electric energy shows the expected theoretical exponential rate of decay up to approximately  $10^{-6}$ . After that level, the low-rank error dominates and we basically enter into a stagnation region (see section 7.2 for simulations with higher ranks). Concerning the errors in mass and in total energy (both quantities are conserved by the original equation), even though the proposed low-rank projector-splitting integrator does not preserve a priori any quantity we obtain conservation up to roughly  $2 \cdot 10^{-8}$  and  $4 \cdot 10^{-8}$  for mass and energy, respectively.

### 6.3. Two stream instability simulation

Let us perform now a simulation with the 6D two stream instability (17) with 128 discretization points for each spatial and velocity variable. The set of parameters is the same as for the example presented in section 6.1, but we integrate the problem until time  $T = 60$  with the second order algorithm with a timestep size of  $\tau = 10^{-2}$ . The rank is fixed to  $r = 10$ . As for the linear Landau problem, we investigate the behavior of the electric energy and the conservation of mass and total energy. The results are summarized in Figure 5. In this case, as expected, the electric energy shows an exponential increase before entering into a saturation phase, and similar considerations apply also for the error in mass and in energy. This matches well with what has been previously reported in the literature for this problem.

## 7. Performance results

We now investigate the performance of the low-rank projector-splitting algorithms presented in section 4. This, in particular, should highlight the efficiency of using our software framework **Ensign** and demonstrate that GPUs provide an efficient way to run such simulations.

To perform a comparison with the A100 we present results on a dual-socket Intel Xeon Gold 6226R CPU based system with  $2 \times 16$  CPU cores and 192 GB of RAM. For parallelizing the code OpenMP is used and the Intel MKL library is employed for matrix and vector operations. For the GPU performance results we use a single NVIDIA A100 graphic card (as described in the previous section) and cuBLAS for BLAS operations. All simulations are conducted in double precision arithmetics.

### 7.1. CPU/GPU comparison

We consider here the linear Landau problem (16) discretized with  $128^3$  points in both space and velocity directions (total number of degrees of freedom  $128^3 \times 128^3$ ). This is done

CPU		GPU	
	Wall-clock time (s)		Wall-clock time (s)
K step	$2.87 \cdot 10^0$	K step	$2.34 \cdot 10^{-2}$
L step	$2.77 \cdot 10^0$	L step	$2.34 \cdot 10^{-2}$
D coefficients	$1.17 \cdot 10^0$	D coefficients	$1.13 \cdot 10^{-2}$
C coefficients	$1.17 \cdot 10^0$	C coefficients	$1.12 \cdot 10^{-2}$
Electric field	$9.76 \cdot 10^{-2}$	QR decomposition K	$5.31 \cdot 10^{-3}$
QR decomposition L	$2.00 \cdot 10^{-2}$	QR decomposition L	$5.26 \cdot 10^{-3}$
QR decomposition K	$1.96 \cdot 10^{-2}$	Electric Field	$2.39 \cdot 10^{-3}$
S step	$6.72 \cdot 10^{-5}$	S step	$7.43 \cdot 10^{-4}$
Total	$8.12 \cdot 10^0$	Total	$8.30 \cdot 10^{-2}$

Table 1: Breakdown of timings for a single step of the first order algorithm, in descending order, for CPU and GPU simulation of a linear Landau problem.

so that the effort of the  $K$  and  $L$  step can be directly compared. We integrate it until final time  $T = 60$  with a timestep size of  $\tau = 10^{-2}$  and rank  $r = 10$ . We report the timings (in descending order) of a single timestep for the relevant parts of the algorithms in Table 1 and Table 2 for the first order and the second order schemes, respectively.

As expected, the most costly parts of the algorithms consist of the  $K$  and the  $L$  steps (with roughly the same computational time, as the degrees of freedom are equal in space and velocity). The cost of the  $S$  step, which involves the solution of a problem of size  $r \times r$  is negligible. The remaining major part of the cost lies in the computation of the  $C$  and the  $D$  coefficients: again, this is expected, as they require a matrix-matrix product of size  $N_v \times r$  (and  $N_x \times r$ , respectively). A single time step of the second order scheme is, as we would expect, approximately twice as costly as the first order scheme.

In both cases, we observe a drastic speedup (up to a factor of 100) between the GPU and the CPU based systems. The main reason for this is that very efficient implementations of matrix-matrix products are available on the GPU (in particular, in cuBLAS). This helps both in computing the coefficients as well as performing the  $K$  and  $L$  step. In addition, our algorithm needs to compute transcendental functions in order to evaluate the matrix functions in Fourier space. This is also an area where the GPU kernels drastically outperform the corresponding CPU implementation.

## 7.2. Varying rank

We now investigate the performances of the GPU implementation for the second order low-rank projector-splitting algorithm for different ranks. For this purpose, we consider again the 6D linear Landau problem (16) with 64 discretization points for each spatial variable and 128 discretization points for each velocity variable. We integrate the problem up to  $T = 60$  with a timestep size of  $\tau = 10^{-2}$  and different ranks  $r = 5, 10, 15, 20$ . The computational times for a single timestep of the simulation are reported in table 3. The wall-clock time

CPU		GPU	
	<i>Wall-clock time (s)</i>		<i>Wall-clock time (s)</i>
Lie splitting	$8.02 \cdot 10^0$	Lie splitting	$8.03 \cdot 10^{-2}$
First K step + QR	$2.83 \cdot 10^0$	First K step + QR	$3.19 \cdot 10^{-2}$
Second K step + QR	$2.82 \cdot 10^0$	Second K step + QR	$2.99 \cdot 10^{-2}$
L step + QR	$2.82 \cdot 10^0$	L step + QR	$2.89 \cdot 10^{-2}$
C coefficients	$1.12 \cdot 10^0$	C coefficients	$1.10 \cdot 10^{-2}$
D coefficients	$1.11 \cdot 10^0$	D coefficients	$1.09 \cdot 10^{-2}$
Electric field	$1.01 \cdot 10^{-1}$	Electric Field	$1.53 \cdot 10^{-3}$
First S step	$5.83 \cdot 10^{-5}$	First S step	$6.81 \cdot 10^{-4}$
Second S step	$5.12 \cdot 10^{-5}$	Second S step	$6.50 \cdot 10^{-4}$
Total	$1.88 \cdot 10^1$	Total	$1.96 \cdot 10^{-1}$

Table 2: Breakdown of timings for a single step of the second order algorithm, in descending order, for CPU and GPU simulation of a linear Landau problem.

increases with increasing rank in a roughly linear fashion. This scaling is better than the theoretical estimates for both computing the coefficients as well as for the  $K$  step (both are quadratic in rank).

	<i>Wall-clock time (s)</i>
Rank 5	$5.12 \cdot 10^{-2}$
Rank 10	$8.70 \cdot 10^{-2}$
Rank 15	$1.28 \cdot 10^{-1}$
Rank 20	$1.85 \cdot 10^{-1}$

Table 3: Timings of a single timestep for the linear Landau simulation with increasing ranks.

In Figure 6 we summarize the behavior of the electric energy, of the error in mass and in total energy for all the ranks considered. We can clearly observe that rank 5 is not enough for the 6D problem under investigation. Starting from rank 10, we see a substantial improvement, in particular in terms of decay of electric energy.

Finally, we repeat a similar experiment with the 6D two stream instability problem (17). In this case, we consider 64 discretization points for each spatial and velocity variable, leading to a total number of degrees of freedom of  $64^3 \times 64^3$ . The problem is then integrated up to  $T = 60$  with a timestep size of  $\tau = 10^{-2}$  and increasing rank  $r = 5, 10, 15, 20$ . The computational times for a single timestep are summarized in table 4, and analogous conclusions as for the linear Landau simulations can be drawn.

We remark that for the linear regime rank 5 still gives very good results in that it perfectly predicts both the growth rate of the instability as well as the time of its onset. Starting at



	<i>Wall-clock time (s)</i>
Rank 5	$1.84 \cdot 10^{-2}$
Rank 10	$3.06 \cdot 10^{-2}$
Rank 15	$4.85 \cdot 10^{-2}$
Rank 20	$7.15 \cdot 10^{-2}$

Table 4: Timings of a single timestep for the two stream instability simulation with increasing ranks.

saturation the rank 5 solution tends to overestimate the electric energy and thus the rank has to be increased. In order to capture saturation a rank 10 simulation is sufficient. If it is desired to integrate far into the nonlinear regime the rank has to be increased further (see Figure 7).

## 8. Conclusions

We have demonstrated, by conducting numerical simulation for two test problems, that six-dimensional Vlasov simulations using a dynamical low-rank algorithm can be efficiently run on GPU based systems. In particular, we report a drastic speedup compared to the CPU implementation and we note that these are the first dynamical low-rank results obtained for the full six-dimensional problem. We also emphasize that results with similar resolution using a direct (Eulerian or semi-Lagrangian) Vlasov solver could only be attained on large-scale supercomputers.

Algorithmic efficiency has been achieved by proposing a CFL-free and second order exponential integrator based dynamical low-rank scheme that uses a Fourier spectral space discretization. Implementation efficiency has been achieved by basing the implementation on the software framework *Ensign*.

## References

- [1] J. Bigot, V. Grandgirard, G. Latu, C. Passeron, F. Rozar, and O. Thomine. Scaling gysela code beyond 32K-cores on bluegene/Q. In *ESAIM: Proceedings*, volume 43, pages 117–135. EDP Sciences, 2013.
- [2] H. Burau, R. Widera, W. Hönig, G. Juckeland, A. Debus, T. Kluge, U. Schramm, T.E. Cowan, R. Sauerbrey, and M. Bussmann. PIConGPU: a fully relativistic particle-in-cell code for a GPU cluster. *IEEE Transactions on Plasma Science*, 38(10):2831–2839, 2010.
- [3] E. Camporeale, G.L. Delzanno, B.K. Bergen, and J.D. Moulton. On the velocity space discretization for the Vlasov–Poisson system: comparison between implicit Hermite spectral and Particle-in-Cell methods. *Computer Physics Communications*, 198:47–58, 2016.
- [4] G. Ceruti and C. Lubich. An unconventional robust integrator for dynamical low-rank approximation. *BIT Numerical Mathematics*, pages 1–22, 2021.

- [5] Intel Corporation. Intel Math Kernel Library. <https://software.intel.com/content/www/us/en/develop/tools/oneapi/components/onemkl>. 2021.
- [6] NVIDIA Corporation. cuBLAS documentation. <https://docs.nvidia.com/cuda/cublas/index.htm>. 2021.
- [7] Z. Ding, L. Einkemmer, and Q. Li. Dynamical Low-Rank Integrator for the Linear Boltzmann Equation: Error Analysis in the Diffusion Limit. *SIAM J. Numer. Anal.*, 59(4):2254–2285, 2021.
- [8] L. Einkemmer. High performance computing aspects of a dimension independent semi-Lagrangian discontinuous Galerkin code. *Computer Physics Communications*, 202:326–336, 2016.
- [9] L. Einkemmer. A low-rank algorithm for weakly compressible flow. *SIAM J. Sci. Comput.*, 41(5):A2795–A2814, 2019.
- [10] L. Einkemmer. A performance comparison of semi-Lagrangian discontinuous Galerkin and spline based Vlasov solvers in four dimensions. *Journal of Computational Physics*, 376:937–951, 2019.
- [11] L. Einkemmer, J. Hu, and Y. Wang. An asymptotic-preserving dynamical low-rank method for the multi-scale multi-dimensional linear transport equation. *J. Comput. Phys.*, 439:110353, 2021.
- [12] L. Einkemmer, J. Hu, and L. Ying. An efficient dynamical low-rank algorithm for the Boltzmann–BGK equation close to the compressible viscous flow regime. *To Appear in SIAM J. Sci. Comput*, 2021.
- [13] L. Einkemmer and I. Joseph. A mass, momentum, and energy conservative dynamical low-rank scheme for the Vlasov equation. *Journal of Computational Physics*, 443:110495, 2021.
- [14] L. Einkemmer and C. Lubich. A low-rank projector-splitting integrator for the Vlasov–Poisson equation. *SIAM Journal on Scientific Computing*, 40(5):B1330–B1360, 2018.
- [15] L. Einkemmer and A. Ostermann. An almost symmetric Strang splitting scheme for non-linear evolution equations. *Computers & Mathematics with Applications*, 67(12):2144–2157, 2014.
- [16] L. Einkemmer and A. Ostermann. An almost symmetric Strang splitting scheme for the construction of high order composition methods. *Journal of Computational and Applied Mathematics*, 271:307–318, 2014.

- [17] L. Einkemmer, A. Ostermann, and C. Piazzola. A low-rank projector-splitting integrator for the Vlasov–Maxwell equations with divergence correction. *Journal of Computational Physics*, 403:109063, 2020.
- [18] V. Grandgirard, Y. Sarazin, X. Garbet, G. Dif-Pradalier, P. Ghendrih, N. Crouseilles, G. Latu, E. Sonnendrücker, N. Besse, and P. Bertrand. Gysela, a full-f global gyrokinetic Semi-Lagrangian code for ITG turbulence simulations. In *AIP conference proceedings*, volume 871, pages 100–111, 2006.
- [19] W. Guo and Y. Cheng. A Sparse Grid Discontinuous Galerkin Method for High-Dimensional Transport Equations and Its Application to Kinetic Simulations. *SIAM Journal on Scientific Computing*, 38(6):A3381–A3409, 2016.
- [20] W. Guo and J.-M. Qiu. A Low Rank Tensor Representation of Linear Transport and Nonlinear Vlasov Solutions and Their Associated Flow Maps. *arXiv:2106.08834*, 2021.
- [21] M. Hochbruck and A. Ostermann. Exponential integrators. *Acta Numerica*, 19:209–286, 2010.
- [22] O. Koch and C. Lubich. Dynamical low-rank approximation. *SIAM J. Matrix Anal. Appl.*, 29(2):434–454, 2007.
- [23] K. Kormann. A semi-Lagrangian Vlasov solver in tensor train format. *SIAM Journal on Scientific Computing*, 37(4):B613–B632, 2015.
- [24] K. Kormann and E. Sonnendrücker. Sparse Grids for the Vlasov–Poisson Equation. In *Sparse Grids and Applications - Stuttgart 2014*, pages 163–190. Springer International Publishing, 2016.
- [25] J. Kusch, G. Ceruti, L. Einkemmer, and M. Frank. Dynamical low-rank approximation for Burgers’ equation with uncertainty. *arXiv:2105.04358*, 2021.
- [26] J. Kusch, L. Einkemmer, and G. Ceruti. On the stability of robust dynamical low-rank approximations for hyperbolic problems. *arXiv:2107.07282*, 2021.
- [27] C. Lubich. *From quantum to classical molecular dynamics: reduced models and numerical analysis*. European Mathematical Society, 2008.
- [28] C. Lubich and I.V. Oseledets. A projector-splitting integrator for dynamical low-rank approximation. *BIT Numerical Mathematics*, 54(1):171–188, 2014.
- [29] H.-D. Meyer, F. Gatti, and G. A. Worth. *Multidimensional quantum dynamics*. John Wiley & Sons, 2009.
- [30] H.-D. Meyer, U. Manthe, and L. S. Cederbaum. The multi-configurational time-dependent Hartree approach. *Chem. Phys. Letters*, 165(1):73–78, 1990.

- [31] R. Nath, Tomov S., and J. Dongarra. Accelerating GPU kernels for dense linear algebra. In *Proceedings of the 2009 International Meeting on High Performance Computing for Computational Science, VECPAR'10*. Springer, 2010.
- [32] Z. Peng, R. G. McClarren, and M. Frank. A low-rank method for two-dimensional time-dependent radiation transport calculations. *Journal of Computational Physics*, 421:109735, 2020.
- [33] Z. Peng and R.G. McClarren. A high-order/low-order (HOLO) algorithm for preserving conservation in time-dependent low-rank transport calculations. *Journal of Computational Physics*, 447:110672, 2021.
- [34] The SeLaLib project team. SeLaLib library. <https://selalib.github.io/>, 2021.
- [35] D. Tskhakaya and R. Schneider. Optimization of PIC codes by improved memory management. *Journal of Computational Physics*, 225(1):829–839, 2007.
- [36] J. P. Verboncoeur. Particle simulation of plasmas: review and advances. *Plasma Physics and Controlled Fusion*, 47(5A):A231–A260, 2005.
- [37] S. Von Alfthan, D. Pokhotelov, Y. Kempf, S. Hoilijoki, I. Honkonen, A. Sandroos, and M. Palmroth. Vlasiator: First global hybrid-Vlasov simulations of Earth’s foreshock and magnetosheath. *Journal of Atmospheric and Solar-Terrestrial Physics*, 120:24–35, 2014.
- [38] Z. Xianyi, W. Qian, and Z. Yunquan. Model-driven level 3 blas performance optimization on loongson 3a processor. In *2012 IEEE 18th international conference on parallel and distributed systems*, pages 684–691. IEEE, 2012.

```

1  /* ... */
2  // Step 1
3  coeff(V0, V0, w_v1, C1v1, blas);
4  coeff(V0, V0, w_v2, C1v2, blas);
5  coeff(V0, V0, w_v3, C1v3, blas);
6  coeff(V0, dV0_v1, h_vv, C2v1, blas);
7  coeff(V0, dV0_v2, h_vv, C2v2, blas);
8  coeff(V0, dV0_v3, h_vv, C2v3, blas);
9  // Step 2
10 blas.matmul(X0, S0, K0);
11 // Step 3
12 /* Compute electric field E0 */
13 // Step 4
14 /* Solve evolution equation for K and store result in K1 */
15 // Step 5
16 gs(K1, S1, ip_xx);
17 X1 = K1;
18 /* ... */
19 // Step 6
20 coeff(X1, X1, w_x1, D1x1, blas);
21 coeff(X1, X1, w_x2, D1x2, blas);
22 coeff(X1, X1, w_x3, D1x3, blas);
23 coeff(X1, dX1_x1, h_xx, D2x1, blas);
24 coeff(X1, dX1_x2, h_xx, D2x2, blas);
25 coeff(X1, dX1_x3, h_xx, D2x3, blas);
26 // Step 7
27 /* Solve evolution equation for S and store result in S2 */
28 // Step 8
29 blas.matmul_transb(V0, S2, L0);
30 // Step 9
31 /* Solve evolution equation for L and store the result in L1 */
32 // Step 10
33 gs(L1, S3, ip_vv);
34 V1 = L1;
35 transpose_inplace(S3);

```

Figure 1: C++ implementation using the **Ensign** framework of the orange colored lines of Algorithm 1.

```

1  for(int k = 0; k < N_xx[2]; k++){
2      for(int j = 0; j < N_xx[1]; j++){
3          for(int i = 0; i < N_xx[0]; i++){
4              double x1 = lim_xx[0] + i*h_xx[0];
5              double x2 = lim_xx[1] + j*h_xx[1];
6              double x3 = lim_xx[2] + k*h_xx[2];
7              X0(i + j*N_xx[0] + k*(N_xx[0]*N_xx[1]), 0) = e11(x1,x2,x3);
8          }
9      }
10 }

```

Figure 2: C++ implementation using the `Ensign` framework of the initialization of a column of the input matrix `X0`.

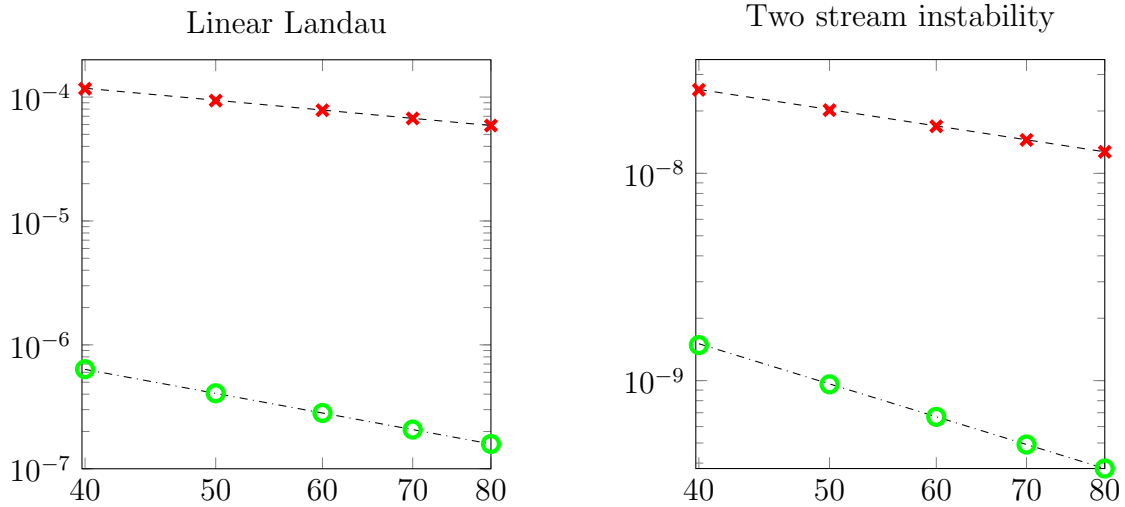


Figure 3: Orders of convergence for first order (red crosses) and second order (green circles) low-rank projector-splitting algorithms. Left plot: linear Landau. Right plot: two stream instability. The (relative) error is computed in maximum norm for a number of timesteps equal to  $m = 40, 50, 60, 70, 80$ . The (relative) error is computed in maximum norm for a number of timesteps equal to  $m = 40, 50, 60, 70, 80$ . The dashed and dashed-dotted lines are reference lines of slope -1 and -2, respectively.

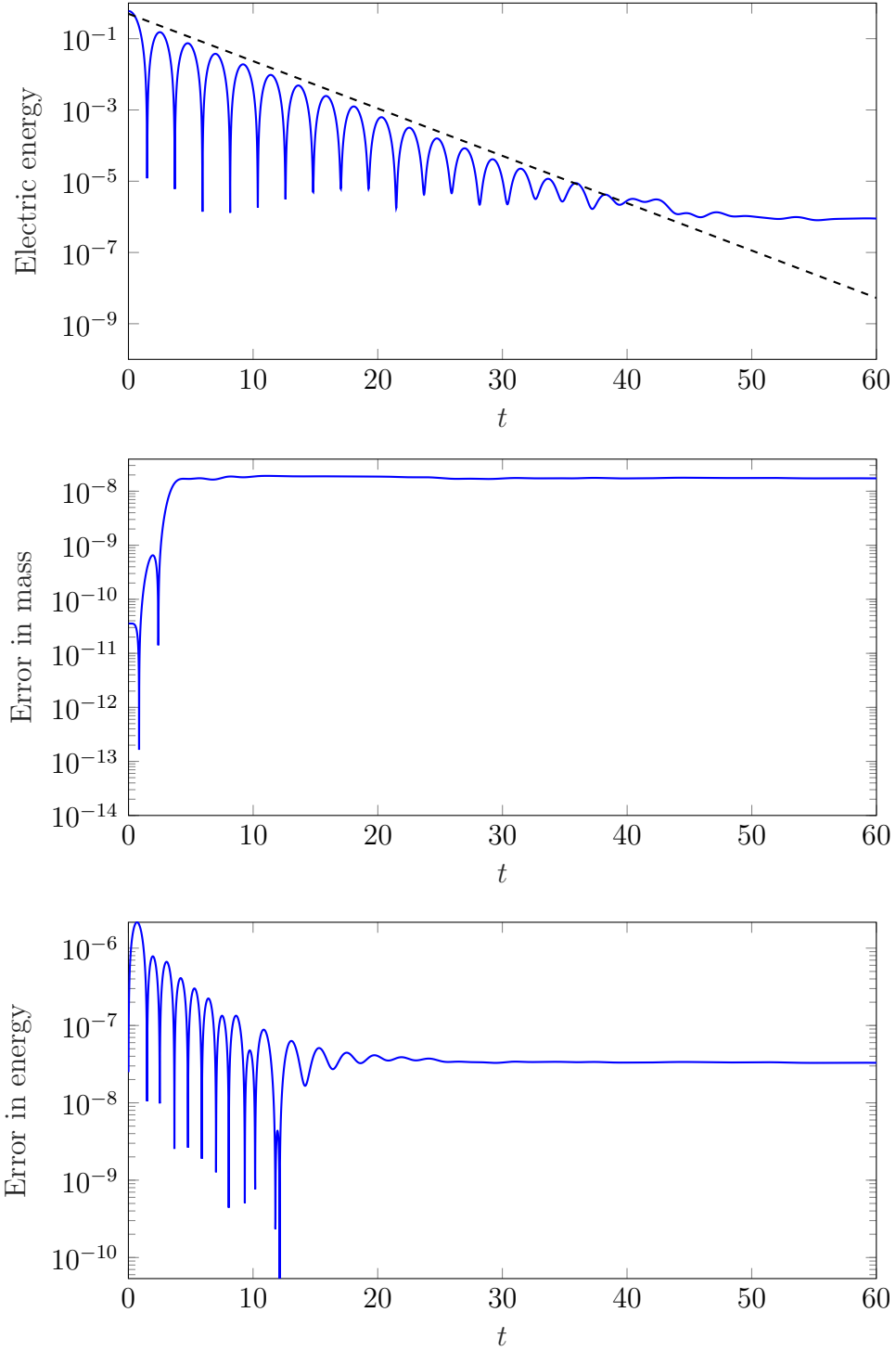


Figure 4: Linear Landau damping simulation with  $64^3 \times 256^3$  degrees of freedom, rank  $r = 10$  and timestep size  $\tau = 10^{-2}$ . The second order low-rank projector-splitting algorithm is employed. Top plot: behavior of electric energy, with reference decay rate. Center plot: error in mass (relative). Bottom plot: error in total energy (relative).

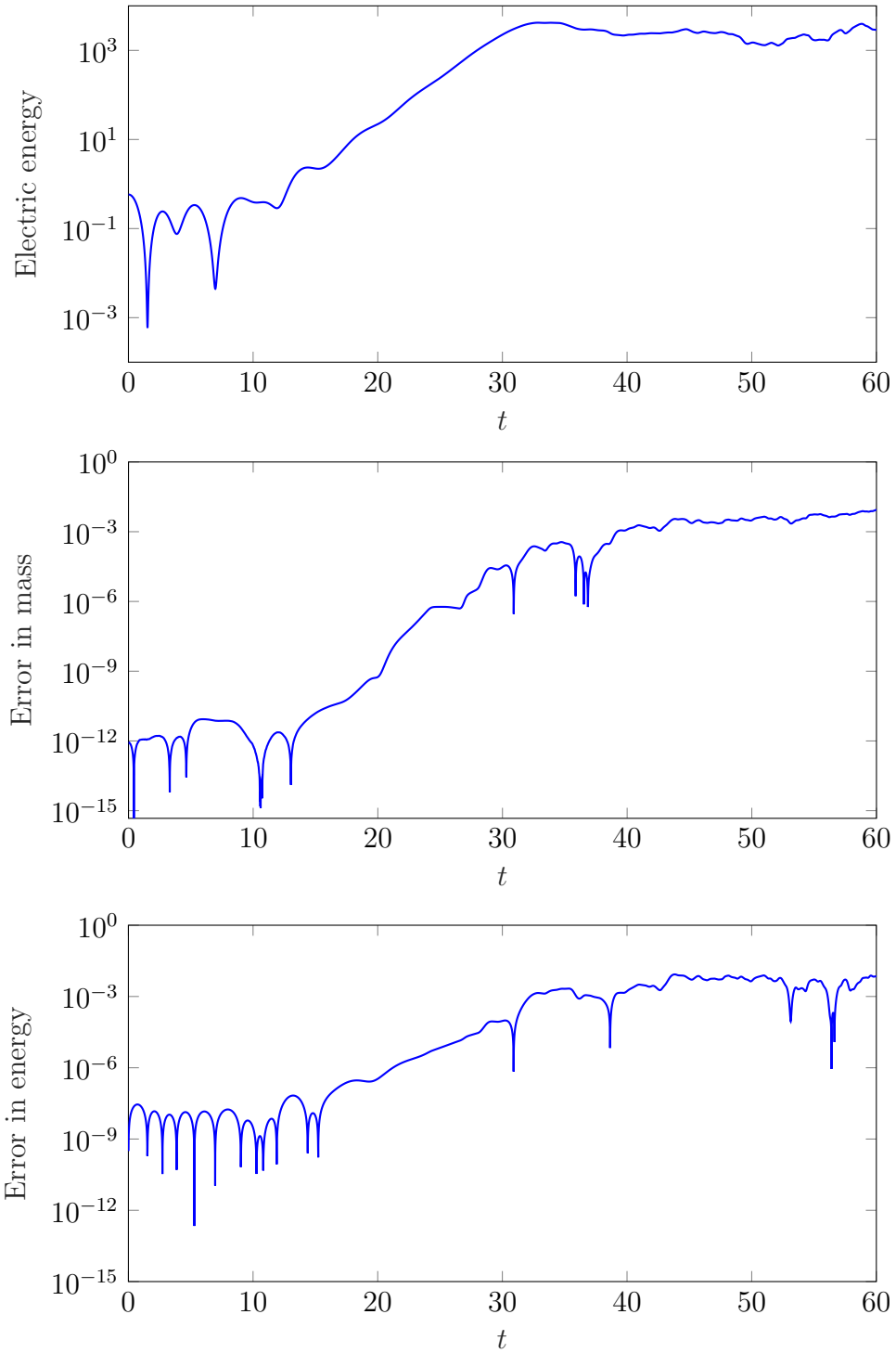


Figure 5: Two stream instability simulation with  $128^3 \times 128^3$  degrees of freedom, rank  $r = 10$  and timestep size  $\tau = 10^{-2}$ . The second order low-rank projector-splitting algorithm is employed. Top plot: behavior of electric energy. Center plot: error in mass (relative). Bottom plot: error in total energy (relative).



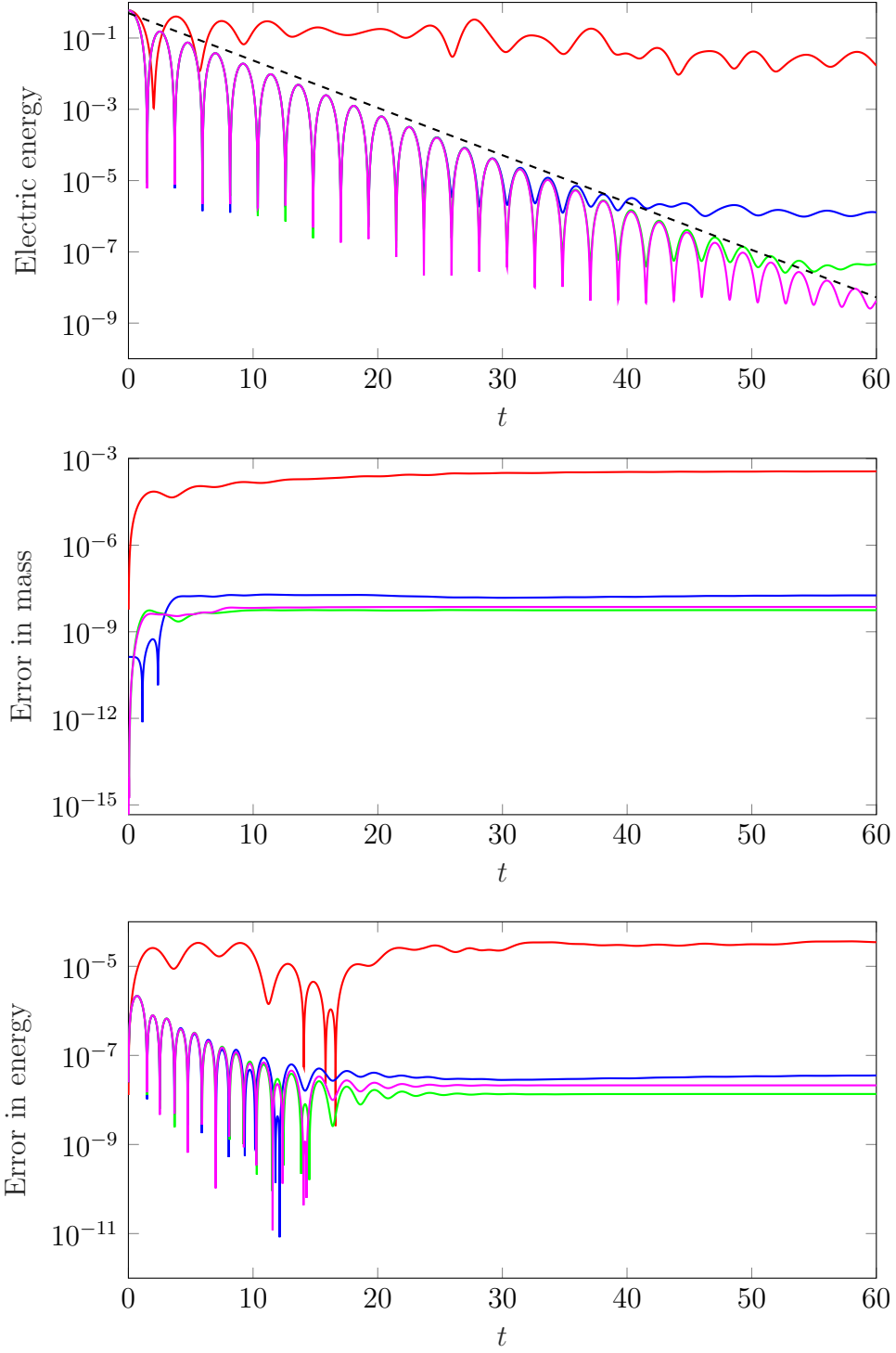


Figure 6: Linear Landau damping simulation with  $64^3 \times 128^3$  degrees of freedom, timestep size  $\tau = 10^{-2}$  and different ranks  $r$ . The second order low-rank projector-splitting algorithm is employed. The red line corresponds to  $r = 5$ , the blue one to  $r = 10$ , the green one to  $r = 15$  and the magenta one to  $r = 20$ . Top plot: behaviour of electric energy, with reference decay rate. Center plot: error in mass (relative). Bottom plot: error in total energy (relative).

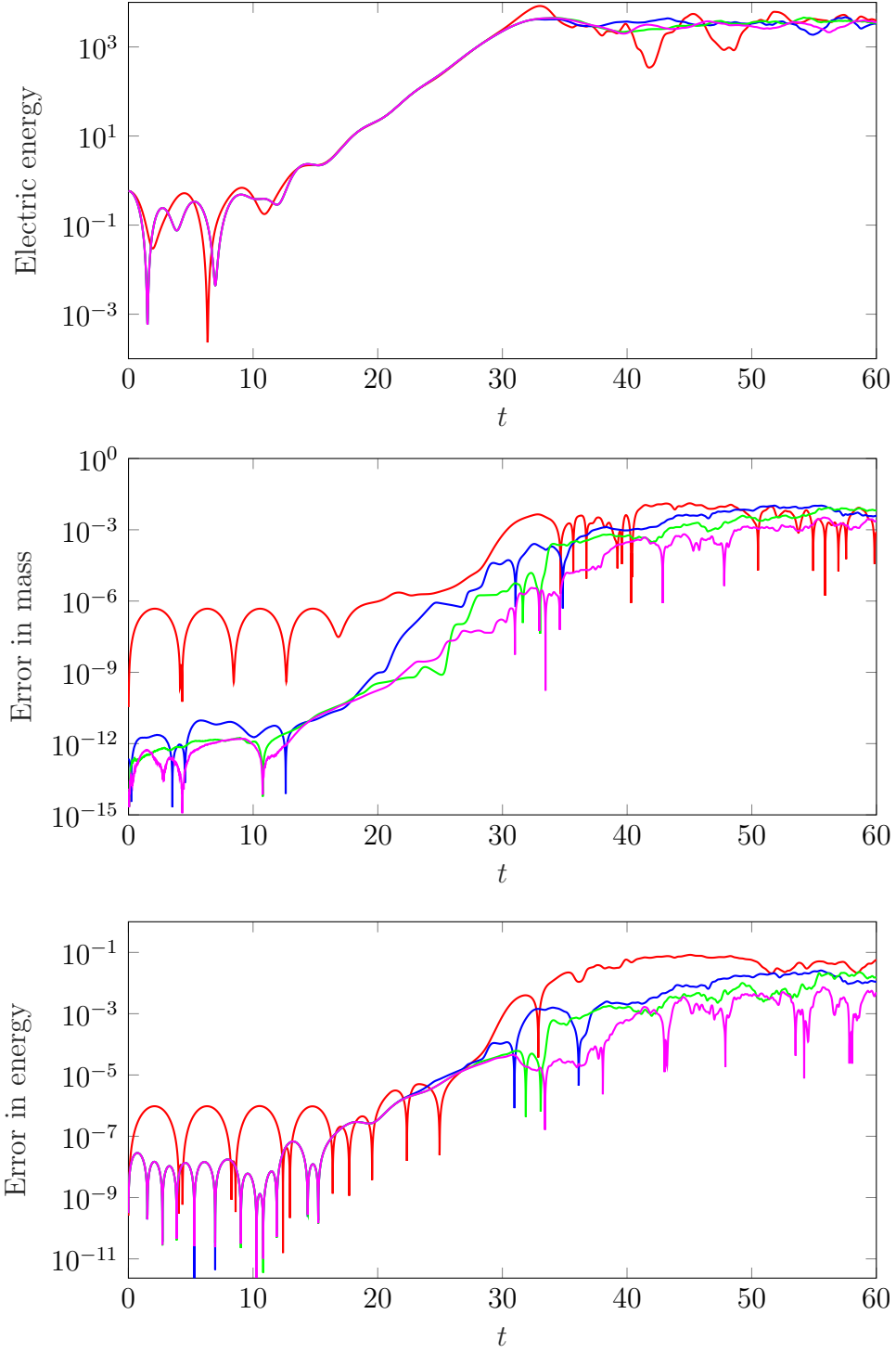


Figure 7: Two stream instability simulation with  $64^3 \times 64^3$  degrees of freedom, timestep size  $\tau = 10^{-2}$  and different ranks  $r$ . The second order low-rank projector-splitting algorithm is employed. The red line corresponds to  $r = 5$ , the blue one to  $r = 10$ , the green one to  $r = 15$  and the magenta one to  $r = 20$ . Top plot: behaviour of electric energy. Center plot: error in mass (relative). Bottom plot: error in total energy (relative).